Open Access Articles

# *The dynamics of pressure and form drag on a sloping headland: Internal waves versus eddies*

The Faculty of Oregon State University has made this article openly available.
Please share how this access benefits you. Your story matters.



| | |
|---|---|
| **Citation** | Warner, S. J., and P. MacCready (2014), The dynamics of pressure and form drag on a sloping headland: Internal waves versus eddies, Journal of Geophysical Research: Oceans, 119, 1554–1571. doi:10.1002/2013JC009757 |
| **DOI** | 10.1002/2013JC009757 |
| **Publisher** | American Geophysical Union |
| **Version** | Version of Record |
| **Terms of Use** | http://cdss.library.oregonstate.edu/sa-termsofuse |

AGU PUBLICATIONS

JGR

Journal of Geophysical Research: Oceans

RESEARCH ARTICLE

10.1002/2013JC009757

# The dynamics of pressure and form drag on a sloping headland: Internal waves versus eddies

**Sally J. Warner[1] and Parker MacCready[2]**

[1]College of Earth, Ocean, and Atmospheric Sciences, Oregon State University, Corvallis, Oregon, USA, [2]School of Oceanography, University of Washington, Seattle, Washington, USA

**Key Points:**
- Tides generate internal waves and eddies as they flow past sloping topography
- Bottom pressure is divided into parts that do and do not contribute to form drag
- Internal waves and eddies remove similar amounts of energy from tidal currents

**Correspondence to:**
S. J. Warner,
swarner@coas.oregonstate.edu

**Citation:**
Warner, S. J., and P. MacCready (2014), The dynamics of pressure and form drag on a sloping headland: Internal waves versus eddies, *J. Geophys. Res. Oceans*, *119*, 1554–1571, doi:10.1002/2013JC009757.

Received 20 DEC 2013
Accepted 31 JAN 2014
Accepted article online 8 FEB 2014
Published online 6 MAR 2014

**Abstract** Topographically generated eddies and internal waves have traditionally been studied separately even though bathymetry that creates both phenomena is abundant in coastal regions. Here a numerical model is used to understand the dynamics of eddy and wave generation as tidal currents flow past Three Tree Point, a 1 km long, 200 m deep, sloping headland in Puget Sound, WA. Bottom pressure anomalies due to vertical perturbations of the sea surface and isopycnals are used to calculate form drag in different regions of the topography to assess the relative importance of eddies versus internal waves. In regions where internal waves dominate, sea surface and isopycnal perturbations tend to work together to create drag, whereas in regions dominated by eddies, sea surface, and isopycnal perturbations tend to counteract each other. Both phenomena are found to produce similar amounts of form drag even though the bottom pressure anomalies from the eddy have much larger magnitudes than those created by the internal waves. Topography like Three Tree Point is common in high latitude, coastal regions, and therefore the findings here have implications for understanding how coastal topography removes energy from tidal currents.

## 1. Introduction

Form drag occurs in the ocean when currents flow over rough topography, which transfers energy and momentum from large to small scales. It is especially relevant in coastal regions where tidal currents are relatively fast and rough topography is abundant. Unlike frictional drag, which is well parameterized within numerical models, form drag is much more difficult to incorporate into numerical models because robust parameterizations of processes which occur at subgrid scales have yet to be fully developed. For instance, *Niwa and Hibiya* [2011] show that barotropic to baroclinic tidal energy conversion within a global tidal model doubled when grid resolution increased from 1/5° to 1/15°. It has also been shown that form drag can be many times larger than frictional drag in locations of rough topography [*Nash and Moum*, 2001; *Edwards et al*., 2004]. We use a numerical model to quantify the tidal form drag that occurs on an isolated, sloping ridge that generates both internal waves and eddies.

Form drag ($D_{\text{form}}$) arises when currents create an asymmetry of bottom pressure across topography. It is calculated as the spatial integral of the product of bottom pressure anomaly ($p'_{bot}$) and topographic slope ($\nabla h$) over a seafloor area ($A$):

$$D_{\text{form}} = -\int_A p'_{bot} \nabla h \, dA. \tag{1}$$

In this paper, bottom pressure fields are used to determine the locations, magnitudes, and timing of form drag at Three Tree Point (TTP), a headland in Puget Sound, WA. It is further explored how different parts of the pressure field, such as vertical perturbations of the sea surface and isopycnals, contribute to form drag. While the energy removed through form drag from the tidal currents at this location only accounts for a very small percentage of the 2.3 TW of energy removed from tides in the coastal seas [*Niwa and Hibiya*, 2011] or the 733 MW of tidal energy flux that enters Puget Sound [*Lavelle et al*., 1988], TTP is typical of topography found in high latitude, coastal regions, and is therefore a representative case for how eddies and internal waves remove energy from tidal currents.

Topographically generated eddies and internal waves are two processes that have traditionally been studied separately. Both phenomena can be identified by vertical perturbations of the sea surface and


© 2014. American Geophysical Union. All Rights Reserved.

isopycnals, but only eddies also have a nonzero potential vorticity, which is how we differentiate the two. Eddies have been observed [*Pingree and Maddock*, 1979; *Geyer and Signell*, 1990; *Li et al*., 2006; *White and Wolanski*, 2008], modeled [*Black and Gay*, 1987; *Signell and Geyer*, 1991; *Warner and MacCready*, 2009; *Callendar et al*., 2011], and studied in the laboratory [*Boyer and Tao*, 1987; *Klinger*, 1994; *Cenedese and Whitehead*, 1999; *Pawlak and MacCready*, 2002] in cases where eddies are created in the absence of internal waves. A wide range of topographically generated internal waves are described by *Baines* [1995], who details steady theory, and by *Garrett and Kunze* [2007], who review internal tide generation in the deep ocean. Within the classification of *Garrett and Kunze* [2007], TTP falls into the category of having quasi steady lee waves, finite depth, supercritical topographic slope with respect to the wave ray slope, and nonlinear blocking [*Warner et al*., 2013]. Studies of internal waves that are most comparable to those generated at TTP include numerical models of tidal flow over topography [*Nakamura et al*., 2000; *Legg and Huijts*, 2006; *Klymak et al*., 2010a] and observations of hydraulically controlled tidal flow over the sill in Knight Inlet [*Farmer and Armi*, 1999a, 1999b; *Klymak and Gregg*, 2001, 2003]. In particular, at the Knight Inlet sill, *Klymak and Gregg* [2001] show that the interaction between recirculating flow on the lee side can enhance the internal waves. However, due to the hydraulically controlled flow and cross-sill density gradients, the circulation at the Knight Inlet sill is different from that observed at TTP where the Froude numbers are subcritical and the background stratification is more spatially constant.

Many large-scale ocean circulation models have begun to implement topographic-dependent drag parameterizations [*Jayne and St. Laurent*, 2001; *Jayne*, 2009; *Arbic et al*., 2010]. These models use quadratic drag laws to parameterize wave drag at topography with a subcritical slope with respect to the wave-ray slope and small tidal excursions compared to the topographic length. As *Klymak et al*. [2010b] point out, these parameterizations do not take into account supercritical topography. Furthermore, as we show here, the dynamics around topography that spawns both internal lee waves and eddies are different from that of ridges which generate internal waves that freely propagate away.

TTP is chosen for this study because it has been researched extensively in the past. *Edwards et al*. [2004] measured the density field over the ridge-like part of TTP and quantified the "internal" form drag, defined as the part of the total form drag that arises from isopycnal height anomalies. *McCabe et al*. [2006] mapped the velocity field surrounding TTP from which they inferred the sea surface height and quantified the "external" form drag, the portion of the form drag due to sea surface height anomalies. In *Warner et al*. [2013], an array of bottom pressure sensors was used to measure the total form drag, which includes both the internal and external portions. The dynamics at TTP have also been investigated theoretically. *MacCready and Pawlak* [2001] developed a theory for form drag generated by steady, stratified flow over an idealized ridge on a sloping side wall. *Warner and MacCready* [2009] explained why form drag can be misleadingly large in oscillatory flow situations. The tilted headland eddy that is created in the lee of TTP has been explored by *Pawlak et al*. [2003], who details its time evolution, and by *Canals et al*. [2009], who describe the isopycnal structure resulting from the eddy tilt. The form drag at TTP is as much as 50 times larger than frictional drag over a flat bottom of equivalent area [*Edwards et al*., 2004]. Furthermore, the form drag has been found to be bigger than what is predicted by a quadratic drag law with an $O(1)$ drag coefficient acting on the headland projected frontal area [*Warner et al*., 2013].

A lot is known about the dynamics at TTP; however, observations cannot map the entire flow field, and therefore we aim to determine the spatial distribution of form drag from eddies and internal waves and to quantify their respective magnitudes. In this study, a numerical model of TTP is used to dissect the pressure field into the parts relevant to form drag to understand how internal lee waves and eddies create form drag and to determine characteristic patterns of their bottom pressure anomaly.

The model setup and the pressure field decomposition are presented in section 2. In section 3, the internal waves and eddies are described using maps of bottom pressure anomalies. Finally, in section 4, the form drag due to the internal waves and eddies is quantified and discussed. A conclusion follows in section 5.

## 2. Methods

### 2.1. Model Setup

The TTP model was developed using the Regional Ocean Modeling System (ROMS), a free-surface, hydrostatic, primitive equation numerical model [*Shchepetkin and McWilliams*, 2005]. The model domain


© 2014. American Geophysical Union. All Rights Reserved.

encompasses the channel in Puget Sound where TTP is located (Figure 1c), extending about 7 km up and downstream of the headland. The model has 100 m horizontal resolution throughout the domain and 20 terrain-following vertical levels that are unevenly spaced with higher resolution near the surface and bottom. The minimum depth was set to be 3 m to avoid wetting and drying of cells. Bathymetric height was collected during a shipboard survey with a side-scanning multibeam echosounder which provided 5 m resolution of the sea floor close to TTP. Further afield, the bathymetry was from the Puget Sound gridded 27 m bathymetry [*Finlayson*, 2005]. The bathymetry was smoothed to avoid excessively steep slopes (Figure 1e).

The TTP model was one-way nested within the 2006 MoSSea Model [*Sutherland et al*., 2011], a regional model of the Salish Sea and the Oregon, Washington, and British Columbia coasts (Figure 1a). The TTP model was run from 24 October 2006 to 31 October 2006, the same time of year as a 2010 companion field study [*Warner et al*., 2013], so stratification was expected to be similar (Appendix A). Tidal currents were also predicted to be nearly the same during the two time periods by a tidal model of Puget Sound [*Lavelle et al*., 1988]. During both the observation and model periods, the mixed-semidiurnal tidal regime shifted from spring to neap (Appendix A). The initial condition and boundary conditions for the TTP model were taken from hourly output of the MoSSea Model and interpolated to the TTP model grid. This provided tidal forcing and stratification of incoming water to the two open boundaries within the TTP model. No atmospheric forcing was used in the TTP model. Turbulence closure was set to be the $k$–$\epsilon$ version of the generic length scale mixing formulation [*Umlauf and Burchard*, 2003] with Canuto-A stability [*Canuto et al*., 2001]. A quadratic drag law with $C_D=3\times10^{-3}$ was used to parameterize bottom stress, and free-slip conditions were used on the vertical walls. At the open boundaries, the free-surface used Chapman boundary conditions [*Chapman*, 1985], the depth-averaged momentum used Flather boundary conditions [*Flather*, 1976], and all other fields used radiation boundary conditions. All these parameters were chosen to match what was used in the MoSSea Model [*Sutherland et al*., 2011]. The six rows of grid cells closest to the open boundaries were nudged to background values with a timescale of 0.1 days for salinity and temperature and 0.5 days for momentum to avoid reflection of waves off of the open boundaries. Snapshots of the flow field were saved every 15 min of model time.

### 2.2. Pressure Decomposition

The pressure within the model can be divided into parts that do and do not contribute to form drag. ROMS is a hydrostatic model, so to decompose the pressure, we begin with the hydrostatic equation:

$$\frac{\partial p}{\partial z}=-\rho g, \tag{2}$$

where $p=p(\mathbf{x},t)$ is the pressure, $\rho=\rho(\mathbf{x},t)$ is the density, $g$ is the gravity, $\mathbf{x}=(x,y,z)$, and $t$ is the time. The coordinates are oriented along the channel, with positive $y$ in the ebb direction and $z$ positive up (Figure 1c). The density can be divided into three parts, $\rho(\mathbf{x},t)=\rho_0+\bar{\rho}(z,t)+\rho'(\mathbf{x},t)$, where $\rho_0$ is a constant background density, $\bar{\rho}(z,t)$ is the horizontally averaged density at every time step, and $\rho'(\mathbf{x},t)$ is the residual. Substituting the density decomposition into (2) and integrating from a vertical position, $z$, to the surface height $\eta$ gives:

$$p(\mathbf{x},t)=g\rho_0\eta-g\rho_0 z+g\int_z^\eta \bar{\rho}(z,t)\,dz+g\int_z^\eta \rho'(\mathbf{x},t)\,dz. \tag{3}$$

The sea surface height can also be decomposed into the parts that arise from the tidal forcing and a residual

$$\eta(x,y,t)=\underbrace{\bar{\eta}(t)+\eta_{inertial}(y,t)+\eta_{KW}(x,t)}_{\text{tidal forcing}}+\underbrace{\eta'(x,y,t)}_{\text{residual}}. \tag{4}$$

Here $\bar{\eta}(t)$ is the domain-averaged sea surface height that varies over a tidal range of 4 m. The second term, $\eta_{inertial}(y,t)$, is an along-channel sea surface height gradient that causes the acceleration of the tides


© 2014. American Geophysical Union. All Rights Reserved.

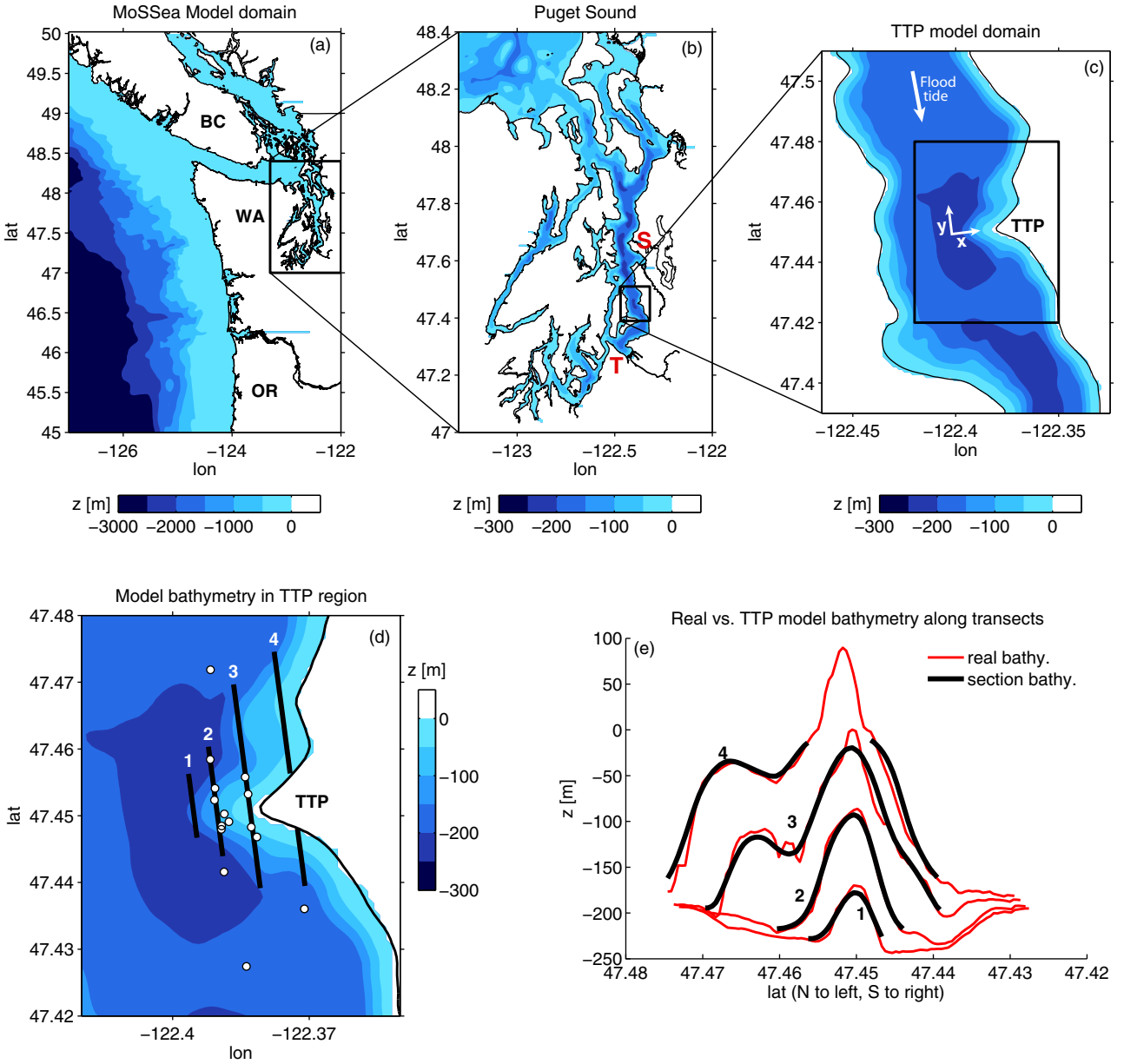


**Figure 1.** (a) MoSSea Model domain and bathymetry. (b) Puget Sound bathymetry. TTP is located about half way between the cities of Seattle (S) and Tacoma (T). (c) TTP model domain and bathymetry. The *x*–*y* coordinate axes are aligned with the across- and along-channel directions. (d) TTP model bathymetry with the four analysis transects. The locations of the bottom pressure sensors (white dots) used in the field study [*Warner et al.*, 2013]. (e) Bathymetric height along the four transects viewed as if looking toward shore, showing real bathymetry (red) and model bathymetry (black).

$$\eta_{inertial}(y,t) = \frac{1}{g}\frac{\partial v_0}{\partial t}(y - y_0), \tag{5}$$

where $y_0$ is a reference location at the center of the channel and $y$ is the along-channel distance from the reference location [*Warner and MacCready*, 2009]. The tidal velocity, $v_0$, flows in the along-channel direction and was calculated from a depth and spatial average of currents from regions about 1 km to the north and south of TTP. The terms in (5) are largest at slack tide with a magnitude of 1 mm km$^{-1}$ and nearly zero at maximum flood and ebb tides. It is included as a separate term because *Warner and MacCready* [2009] show that this background tilting of the sea surface can account for form drag that has a large amplitude, but does no tidally averaged work on the flow because its phase is in quadrature with the velocity. The third term in (4), $\eta_{KW}(x,t)$, is a cross-channel tilt of the sea surface of


© 2014. American Geophysical Union. All Rights Reserved.

up to 2 mm km$^{-1}$ that arises as the tidal wave propagates downstream along the channel banks as a Kelvin wave (approximated with a linear tilt because the 5 km wide channel is much narrower than the 300 km barotropic Rossby radius of deformation):

$$\eta_{KW}(x,t)=\frac{f}{g}v_0(x-x_0). \tag{6}$$

Here, $f$ is the Coriolis frequency and $x_0$ is a reference location in the center of the channel. It cannot affect form drag because it varies perpendicularly to the flow. It is included as a separate term because its removal allows us to more clearly isolate the dynamic part of the sea surface height field, $\eta'(x,y,t)$. The inertial (5) and Kelvin wave (6) terms are quantified by the tidal acceleration and velocity, respectively. We could have simply measured the along and across-channel sea surface slopes to find these terms, but the definitions here prevent the influence of sea surface perturbations which we do not want to include in $\eta_{inertial}$ and $\eta_{KW}$.

By substituting (4) into (3), the following expression for pressure is obtained:

$$p=\underbrace{\underbrace{\underbrace{-\rho_0 gz}_{\text{depth}}+\underbrace{g\int_z^{\eta}\bar{\rho}\,dz}_{\text{backgr. strat.}}}_{\text{static pressure}}+\underbrace{\underbrace{\underbrace{g\rho_0\bar{\eta}}_{\text{tide hgt.}}+\underbrace{g\rho_0\eta_{inertial}}_{*\text{inertial}}+\underbrace{g\rho_0\eta_{KW}}_{\text{Kelvin wave}}}_{\text{tidal forcing}}+\underbrace{\underbrace{g\rho_0\eta'}_{*\text{external}}+\underbrace{g\int_z^{\eta}\rho' dz}_{*\text{internal}}}_{\text{dynamicresidual}}}}. \tag{7}$$

In this equation, only the starred terms contribute to form drag even though they are many orders of magnitude smaller than most of the other terms. The depth, background stratification, and tide height terms have magnitudes that reach $2\times10^6$, $1\times10^3$, and $4\times10^4$ Pa, respectively. The inertial, Kelvin wave, external, and internal terms all have maximum magnitudes of about 150 Pa (Figures 2 and 3). The sum of the internal and external pressures will be called the "dynamic" pressure anomaly because it is the part of the pressure field that does tidally averaged work on the flow and is associated with internal waves and eddies:

$$p'_{\text{dynamic}}=p'_{\text{external}}+p'_{\text{internal}}. \tag{8}$$

Here pressure anomalies are indicated with primes. The sum of the terms that are both time and spatially dependent is the "total" pressure anomaly:

$$p'_{\text{total}}=p'_{\text{external}}+p'_{\text{internal}}+p'_{\text{inertial}}+p'_{\text{Kelvin wave}}. \tag{9}$$

All of these parts of the pressure field are shown in Figures 2 and 3 during flood and slack tides.

### 2.3. Calculating Form Drag

The along-channel component of form drag per unit cross-channel distance is the $y$-integral of seafloor pressure times topographic slope

$$D_{\text{form}}=-\int_{y_1}^{y_2}p'_{bot}h_y\,dy, \tag{10}$$

where $h$ is the topographic height, $h_y$ is the topographic slope in the along-channel direction, and $y_1$ and $y_2$ are locations of equal depth on either side of the topography. The bottom pressure anomaly, $p'_{bot}$, is the pressure in (9) evaluated at the sea floor. Form drag has units of N m$^{-1}$. The form drag in (10) can be calculated with any individual parts of the bottom pressure anomaly in (8) or (9) to get the "inertial drag," "external drag," "internal drag," and "dynamic drag." Only the along-channel component of the form drag is encompassed by (10). *MacCready and Pawlak* [2001] state that form drag must be integrated between points of equal depths. Therefore, it becomes impossible to calculate the across-channel component of form drag over shore-bound topography like TTP with (10). However, we assume that the along-channel


© 2014. American Geophysical Union. All Rights Reserved.

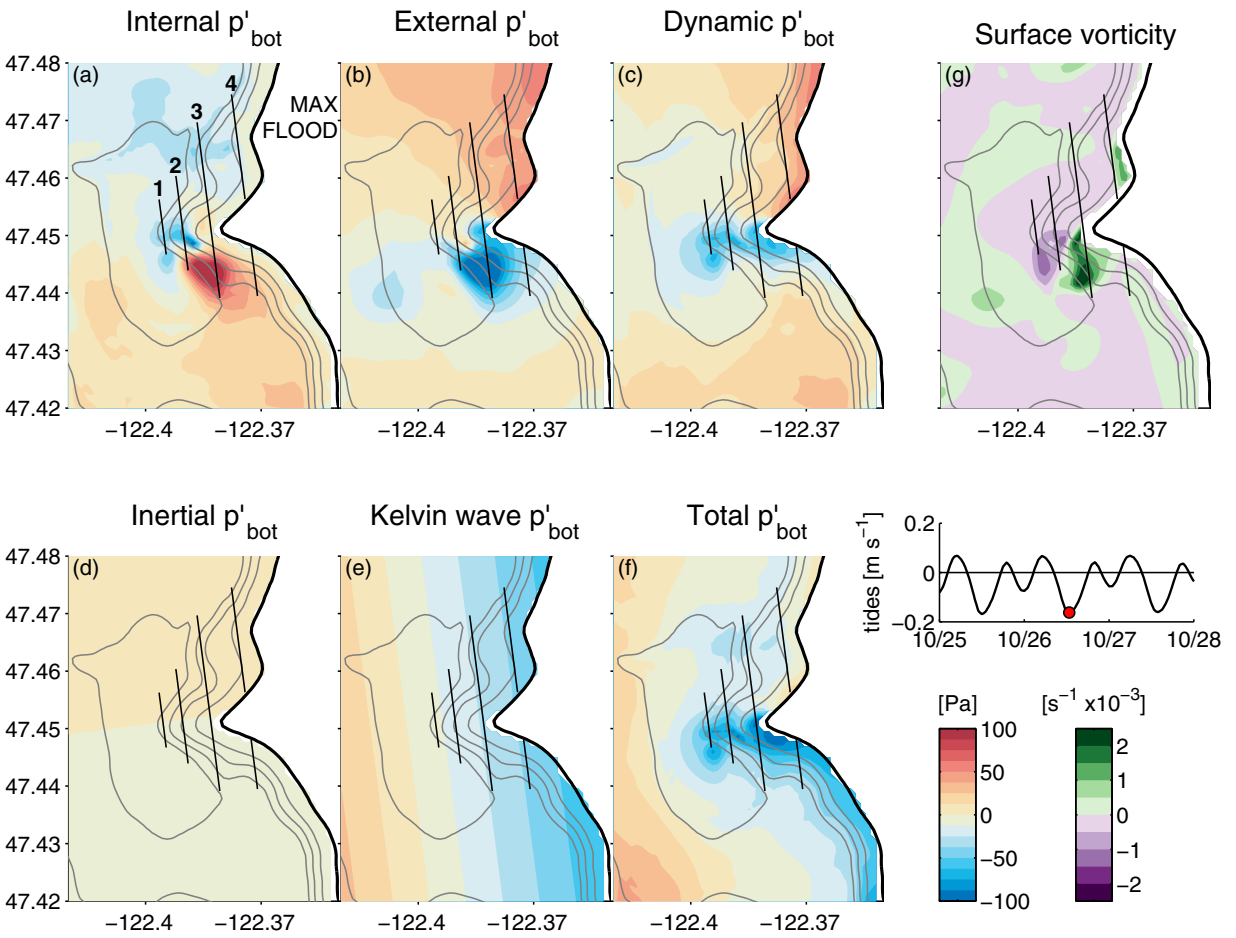


**Figure 2.** (a–f) Bottom pressure anomalies and (g) vorticity at maximum flood tide. The pressure anomaly has been broken up into (a) internal, (b) external, (c) dynamic (equation (8)), (d) inertial, (e) cross-channel Kelvin wave, and (f) total bottom pressure anomalies (equation (9)). Depth contours (gray) every 50 m. Four analysis transects are labeled in Figure 2a. (lower right) Tidal currents ($v_0$) with maximum flood tide indicated with a red dot.

component encompasses most of the form drag because the tidal velocity flows in the along-channel direction and therefore the biggest pressure gradients are in the along-channel direction.

We follow [*Gill*, 1982, section 8.7] and define the power extracted from the tides by the form drag as the product of the form drag and the tidal velocity

$$P_{\text{form}} = D_{\text{form}}\, v_0, \tag{11}$$

which has units of W m$^{-1}$ of channel width. These definitions of form drag and power are with respect to time. We specify tidal averages with $\langle\cdot\rangle$, always being sure to calculate tidal averages over complete tidal cycles. The tidal velocity, $v_0$, is the appropriate velocity to use when calculating power as discussed below.

Four transects that run parallel to the channel were chosen on which to calculate form drag (Figure 1d). The transects were specifically chosen to encompass the parts of topography with nonzero slopes and to end at equal depths (Figure 1e). They are numbered 1–4 from offshore to onshore. Transects 2 and 3 correspond to the ridge and headland transects in the observations, respectively [*Warner et al.*, 2013]. The form drag and power from the model and observations along transect 2 exhibit similar patterns of largest energy conversion during strong flood tides (Appendix A). Both the form drag and power can be divided by the length of each transect, $L$, to get spatial averages in N m$^{-2}$ and W m$^{-2}$, respectively.


© 2014. American Geophysical Union. All Rights Reserved.

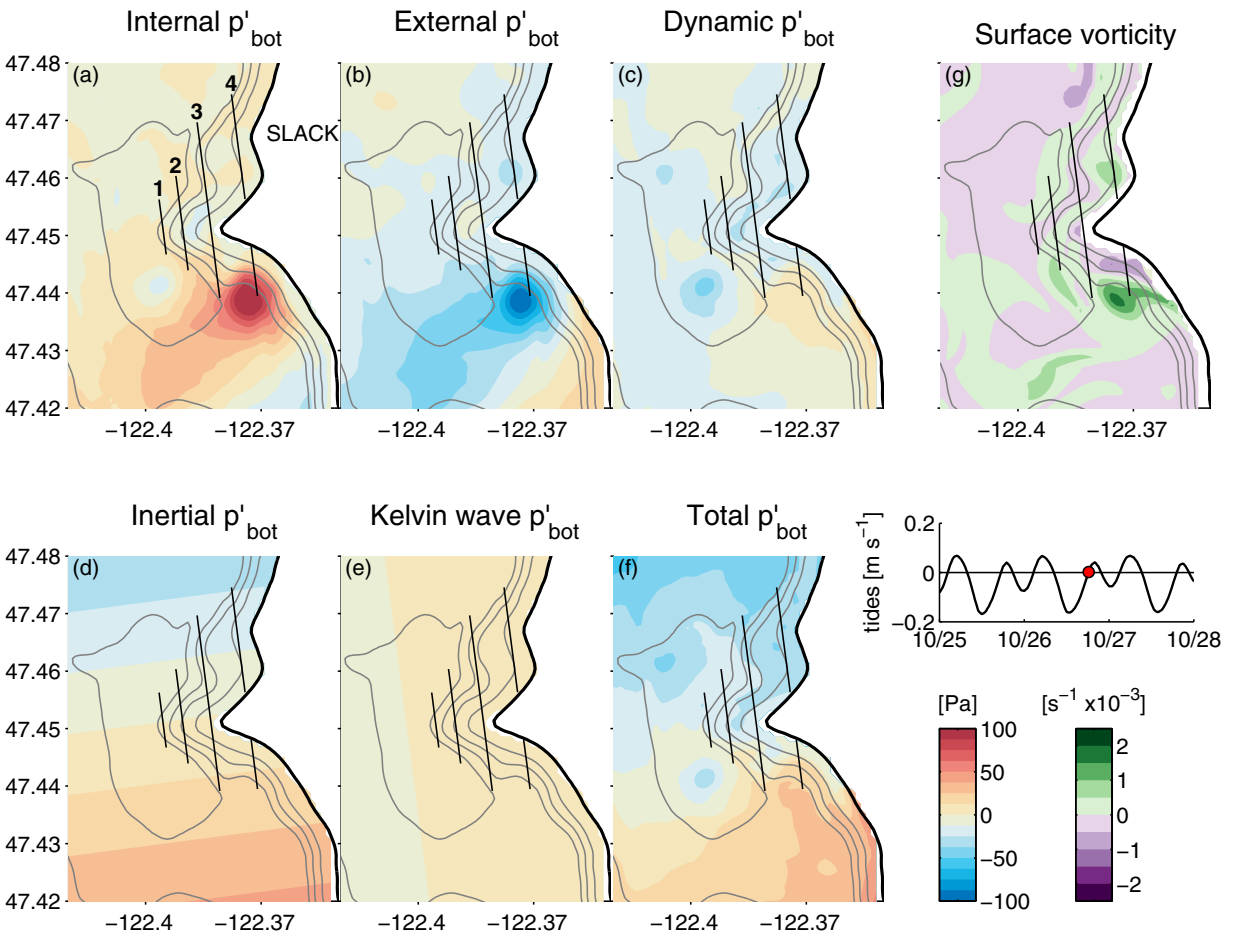


**Figure 3.** (a–f) Bottom pressure anomalies and (g) vorticity at slack tide.

It should be noted that the power (11) differs from the barotropic to baroclinic energy conversion that is commonly used to quantify the energy removed from tides by linear internal wave generation [*Kelly et al.*, 2010, equation (24)]:

$$C_T = -(U, V) \cdot \nabla h p''|_{z=-h}. \tag{12}$$

Here $(U, V)$ are the across and along-channel components of the depth averaged velocity. Unlike $v_0$, which is a channel average, $U$ and $V$ are defined at every grid box. The baroclinic bottom pressure anomaly $(p''_{bot})$ as defined by *Kelly et al.* [2010, equation (42)] differs from $p'_{bot}$ because an additional depth mean has been removed.

Barotropic to baroclinic conversion (12) can be integrated along the four transects and compared to form drag power (11) as shown in Figure 4. The integral of (12) is calculated as

$$C_{Ty} = \frac{1}{L}\int C_T dy, \tag{13}$$

which has units of W m$^{-2}$. Along section 1, which is dominated by internal waves and not affected by eddies, both $P_{form}/L$ and $C_{Ty}$ show peaks during strong flood tides. Along sections 3 and 4, which contain eddies but not internal waves, $C_{Ty}$ is substantially smaller than $P_{form}/L$. Time averages of $C_{Ty}$ and $P_{form}/L$ are calculated (Table 1). Along section 1, $<C_{Ty}>$ and $<P_{form}/L>$ are nearly equal, whereas elsewhere on the topography where eddies are present, $<C_{Ty}>$ has a much smaller magnitude than $<P_{form}/L>$.


© 2014. American Geophysical Union. All Rights Reserved.

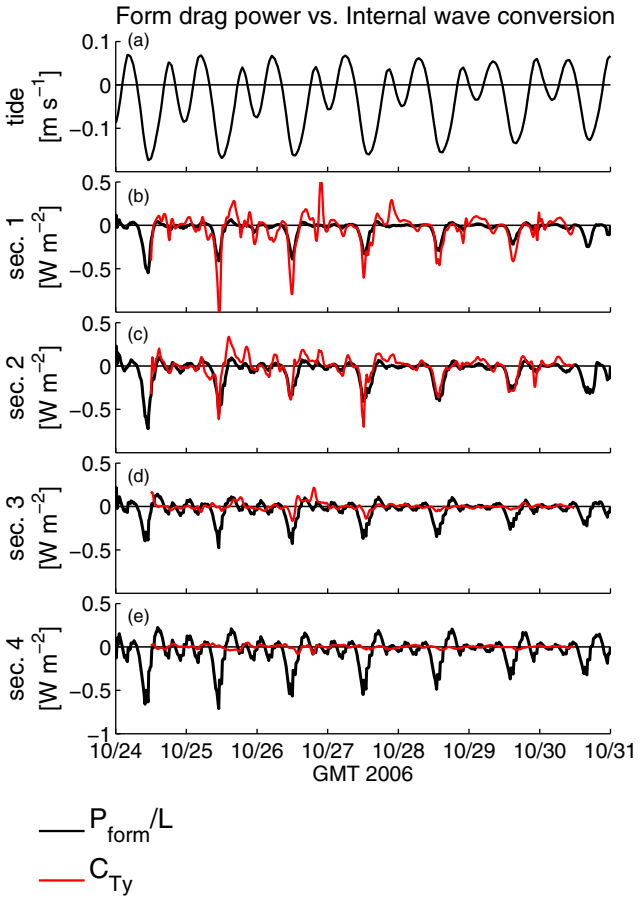


**Figure 4.** (a) Tidal currents. (b–e) Power (equation (11), black) and barotropic to baroclinic conversion (equation (13), red) integrated in space along the four analysis sections and divided by the total section length to get units of W m$^{-2}$. (b) Section 1 is offshore over the more ridge-like part of the topography. (c–e) The next three sections move progressively toward shore.

One of the most important ways that energy is removed from the large-scale flow at TTP is through eddies, which is a form of energy conversion that can be both barotropic and baroclinic. Since (12) only accounts for barotropic to baroclinic conversion, (11) is the more appropriate way to quantify energy lost from the tides at TTP.

## 3. Physical Mechanisms That Create Form Drag

Throughout the next two sections, the relationship between the internal and external pressures within eddies and internal lee waves will be examined to understand how these phenomena contribute to form drag. There are repeated patterns of pressure seen at TTP from one tidal cycle to the next. During flood tide (Figure 2), there are large internal, external, and dynamic bottom pressure anomalies. The inertial bottom pressure is zero and the Kelvin wave pressure has its maximum across-channel gradient. Similar, but reversed, patterns are seen during ebb tide. However, since ebb currents are weaker than flood currents [*Warner et al*., 2013], this analysis focuses on the flood tide. During slack tide (Figure 3), there are still large internal and external pressure anomalies in the domain due to the persistence of an eddy that was created during the previous flood tide. At this time, the internal pressure field has its largest along-channel gradient and the Kelvin wave pressure is zero.

### 3.1. Eddies

Due to the fact that the eddies are being created by sloping topography, the eddies themselves are tilted [*Canals et al*., 2009]. Eddies can be identified by patches of high-magnitude relative vorticity (Figure 2g). The position of the eddy can be tracked through time (Figure 5) by finding the maximum vorticity at the surface and at the bottom as shown with maps of surface and bottom vorticity in Figure 6c. The eddy begins to form about 2 h before maximum flood tide. Even at this early stage, the vorticity maximum at the surface is located much closer to the shore than the vorticity maximum at depth. As the tide gains strength, the eddy is stretched further due to velocity shear, eventually reaching its maximum horizontal displacement between surface and bottom of 1.7 km—equivalent to three eddy diameters—about 4 h following the peak of flood tide. With this separation between surface and bottom, the eddy has a slope of about 1:7 (rise:run). The eddy remains stretched throughout its lifespan even once it is advected by currents away from the headland. *Canals et al*. [2009] show that the velocity remains almost entirely horizontal. TTP is not the only place to spawn tilted eddies. *Oke and Griffin* [2011] describes a tilted eddy off the coast of Australia that has a 100 km diameter and a core that is offset by 28 km over a depth of 4.5 km.

The tilt of the eddy leads to different isopycnal structures and bottom pressure anomalies than are found in a vertical eddy, which in turn can affect how much form drag the eddy creates. A vertical section that goes through the eddy (Figure 6c) shows isopycnal contours that are depressed over the bottom half of the eddy


© 2014. American Geophysical Union. All Rights Reserved.

**Table 1.** Time Averages of Form Drag Power ($<P_{form}/L>$, Equation (11)) and Barotropic to Baroclinic Conversion ($<C_{Ty}>$, Equation (13)) Along the Four Analysis Transects[a]

| Transect | $<P_{form}/L>$ (W m$^{-2}$) | $<C_{Ty}>$ (W m$^{-2}$) |
|---|---|---|
| 1 | −0.0398 | −0.0362 |
| 2 | −0.0541 | −0.0067 |
| 3 | −0.0353 | +0.0010 |
| 4 | −0.0478 | −0.0004 |

[a]Only along transect 1 are the two quantities approximately equal.

and elevated in the top half. At the surface, there is a balance between the centripetal force of the currents and a radial pressure gradient, which can be written with the frictionless, steady shallow-water momentum equation in polar coordinates as

$$-\frac{u_\theta^2}{r} = -g\frac{\partial \eta}{\partial r}, \tag{14}$$

where $u_\theta$ is the azimuthal velocity and $r$ is the radial coordinate. Coriolis acceleration is omitted from (14) because it is an order of magnitude smaller than the centripetal acceleration. The angular currents of the eddy create a depression of the sea surface. Directly below this surface depression the centripetal acceleration is smaller because the vorticity is weaker and there is upward heaving of the isopycnals to balance the low surface pressure. Integrated to the bottom, there is a strong negative external pressure of −129 Pa and a strong positive internal pressure of 122 Pa at this location (Figures 6d and 6e). Even though the internal and external pressure anomalies are large, the dynamic pressure anomaly is nearly zero (Figure 6f). Only close to shore, in water shallower than 50 m where isopycnals cannot be raised enough to compensate for the low external pressure is there a nonzero dynamic pressure anomaly that has a magnitude $>-50$ Pa.

In the bottom half of the eddy, perturbations of the sea surface do not play a role like they do in the top half of the eddy. Here there is a local balance of the centripetal force of the currents and the internal pressure field, which causes isopycnals to be drawn down. Therefore, both internal and external pressure anomalies are negative and they combine to a dynamic pressure of −61 Pa. The opposing forces that pull isopycnals up in the top half of the eddy and down in the bottom half can lead to vertical isopycnal excursions of 50 m as seen for the 1024.1 kg m$^{-3}$ isopycnal (Figure 6c). The bottom half of the eddy, therefore, has a dynamic bottom pressure anomaly that is often just as large as the dynamic pressure anomaly in the top half of the eddy.

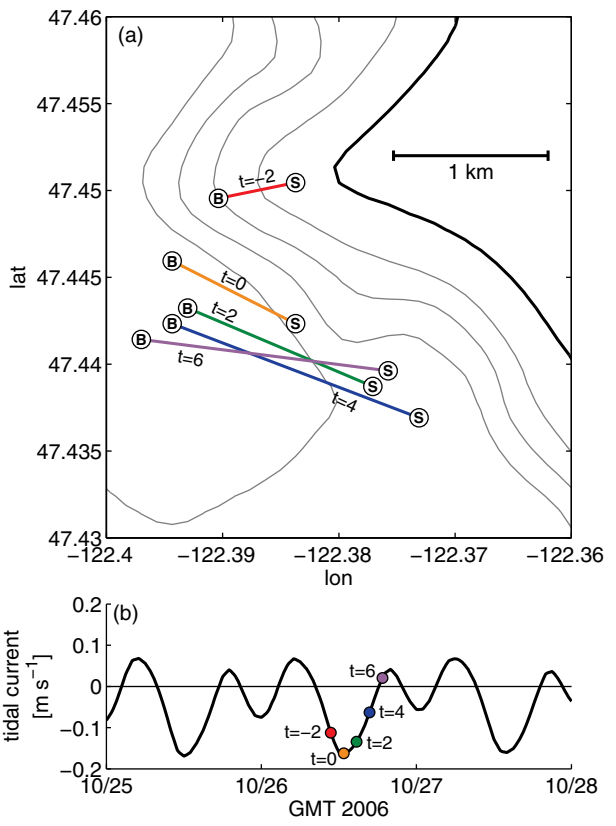


**Figure 5.** (a) The location of the surface (S) and bottom (B) of a lee eddy during a single flood tide plotted every 2 h starting 2 h before maximum flood tide and ending 6 h after maximum flood tide. Depth contours every 50 m. (b) Tidal currents.

During slack tide (Figure 3), the eddy from the previous flood has the largest pressure anomalies within the domain. However, there is nearly complete compensation between the internal and external pressures which leads to a near-zero dynamic pressure anomaly.

Overall, due to the tilted nature of the eddies at TTP, the isopycnals in the upper half of the eddy deviate upward to counteract the negative pressure anomaly at the surface, and in the lower half of the eddy, the isopycnals are depressed downward. Therefore, the eddy only contributes to form drag in two places: at its base where the external pressure does not counteract the internal pressure and in regions that are


© 2014. American Geophysical Union. All Rights Reserved.

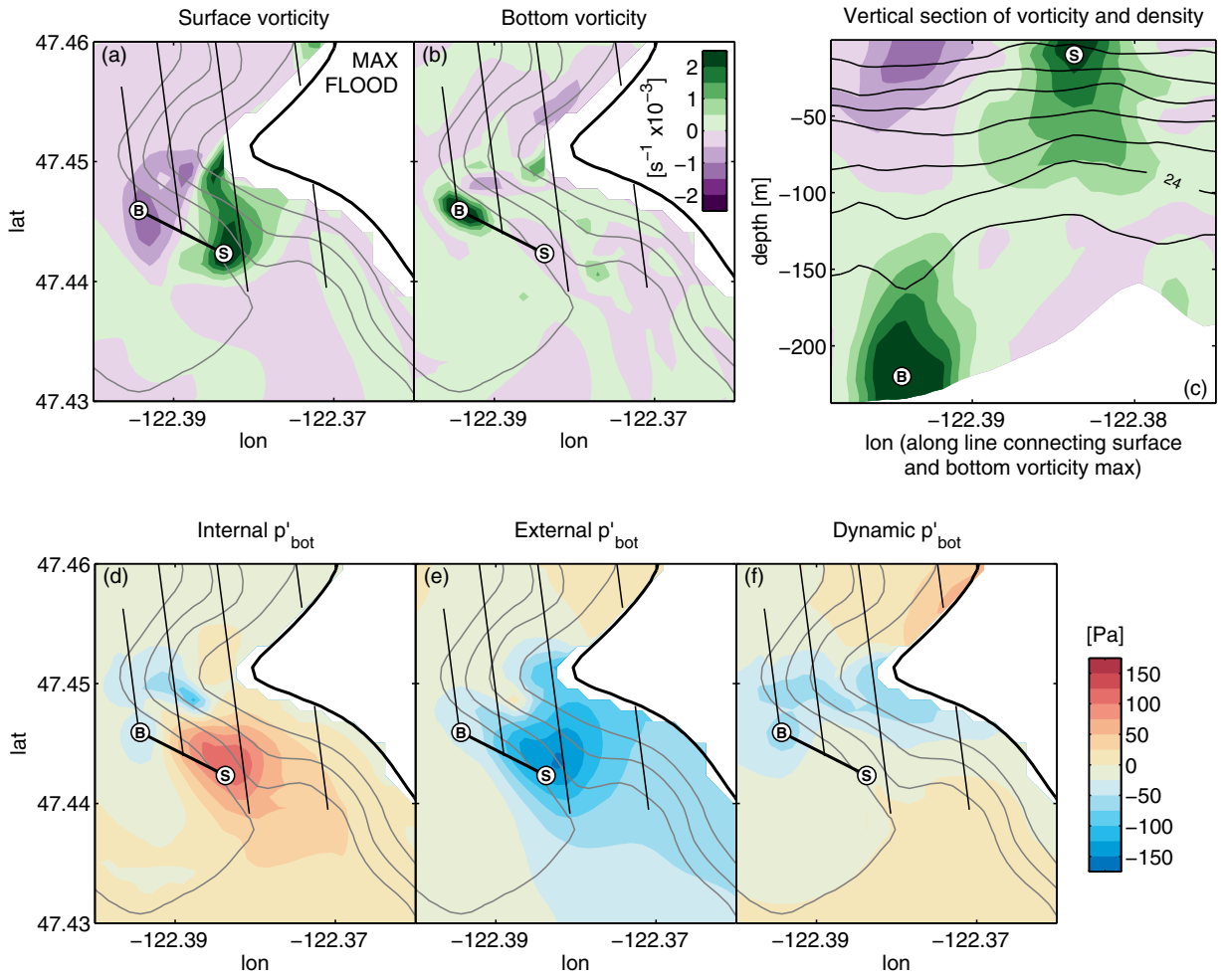


**Figure 6.** (a) Surface vorticity at maximum flood tide, overlaid with depth contours every 50 m (gray) and four analysis transects (thin black). The locations of the maximum surface vorticity (S) and the maximum bottom vorticity (B) are labeled in every subplot. (b) Vorticity in the bottom grid cells. (c) Vertical section of vorticity (color contours) overlaid with potential density contours (black) along a straight line that connects the surface and bottom vorticity maxima. Potential density contours are shown every 0.1 kg m$^{-3}$ and the 1024 kg m$^{-3}$ isopycnal is labeled. (d) Internal bottom pressure anomaly. (e) External bottom pressure anomaly. (f) Dynamic bottom pressure anomaly.

too shallow for the isopycnal excursions to counteract the external pressure. The internal and external pressures associated with an eddy have much larger magnitudes than the dynamic bottom pressure. Therefore, the external form drag measured by *McCabe et al.* [2006] should not be assumed to be the same size as the total form drag, which is much smaller.

### 3.2. Internal Waves

Internal lee waves are generated on the ridge-like part of TTP [*Edwards et al.*, 2004]. Their structure can be investigated by looking at vertical slices of density and bottom pressure along the four transects (Figure 7) to determine how they contribute to form drag. During flood tide along section 1, there is a lee wave on the south side of the topography that has a negative internal pressure anomaly (Figures 7a and 7e). Unlike a classical mode 1 internal wave where the surface perturbations are in the opposite direction as the isopycnal perturbations, here, the external and internal pressures are both negative.

Along section 2 during flood tide, there is an internal wave with a negative internal pressure anomaly visible on the crest of the topography (Figures 7b and 7f). This negative internal pressure exists both upstream and downstream of the topographic crest, but the signal has a greater magnitude on the lee side of −66 Pa. Just like the internal wave on section 1, the external pressure does not counteract the internal pressure. The internal wave along section 2, however, is dwarfed by the positive internal pressure of 59 Pa and negative external pressure of −92 Pa located farther downstream. This is the pressure signal of an eddy that is mostly


© 2014. American Geophysical Union. All Rights Reserved.

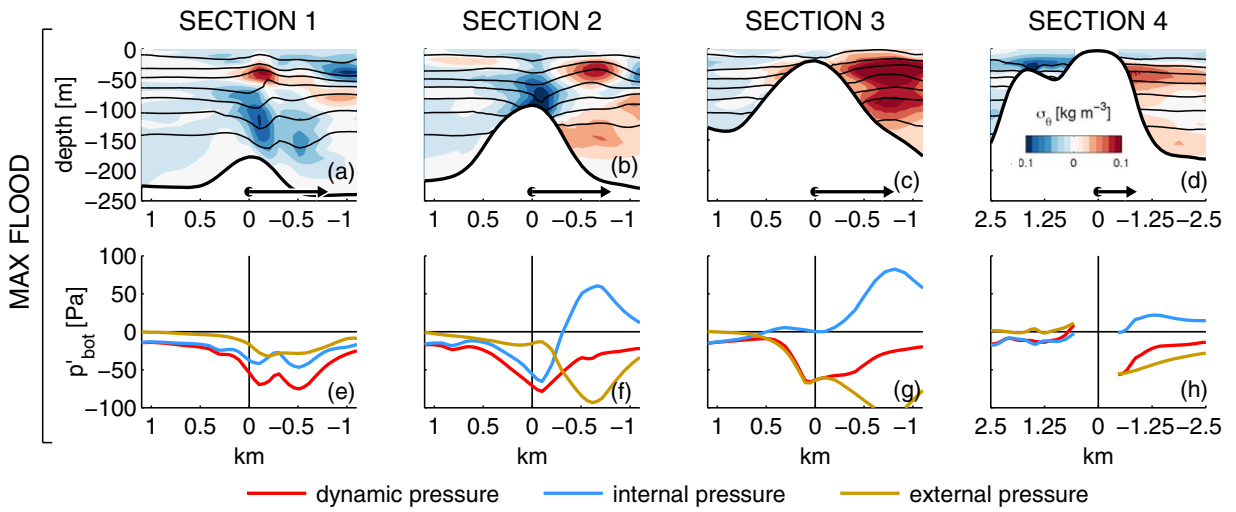


**Figure 7.** Density anomaly overlaid with contours of isopycnal height (a–d) during flood tide along four transects. Density contours every 0.1 kg m$^{-3}$. (e–h) Internal, external, and dynamic bottom pressure anomalies. (Note the different *x* axis scale along section 4).

situated on transect 3 but impinges on the very south end of transect 2 (Figures 2a and 2b). Along sections 3 (Figures 7c and 7g) and 4 (Figures 7d and 7h), the topography is too tall with respect to the water column depth to create internal waves.

Throughout most of the tidal cycle, the eddies and internal waves at TTP stay spatially separated, however, shortly after maximum flood tide, the eddy advects toward the internal lee wave altering the dynamics. Along transects 1 and 2, the internal waves are the dominant mechanism for removing energy from the tides as was shown in Figure 4. When the eddy moves onto these transects, the positive internal pressure anomaly of the eddy confines the negative internal pressure anomaly of the internal waves to a shorter down-stream extent. Along transect 1, where the eddy is not present, the internal wave creates pressure anomalies as far as 750 m downstream. Along transect 2, the internal wave can only depress isopycnals as far as 200 m beyond the topographic crest because the eddy is located just downstream. This changes the sign of the internal form drag because the negative pressure anomalies from the internal lee wave are now located at the crest of the topography and the positive internal pressure anomalies from the eddy are now located over the slope. At Knight Inlet, *Klymak and Gregg* [2001, 2003] describe a situation where internal lee waves are affected by lateral recirculation. The recirculation can account for 25% of the flow thereby increasing the size of the internal lee waves. Unlike the internal lee waves at Knight Inlet, we do not suspect that the flow here is hydraulically controlled. The Froude number stays well within the subcritical range along section 1 $(Fr=v_0/(N(H-h_0)/\pi) \leq 0.54)$. Furthermore, at Knight Inlet, the recirculation is located in a layer of fluid directly on top of the internal wave [*Klymak and Gregg*, 2001]. Therefore, unlike *Klymak and Gregg* [2003] who suggest that the recirculation strengthens the internal wave, here we conclude that the eddy impedes the formation of the internal wave reducing its form drag.

In summary, internal lee waves are generated during flood tides on the more ridge-like part of TTP. They start to form about 2 h before maximum flood tide and remain attached to the topography until the tidal currents slacken sufficiently to release the wave, which occurs about 3 h after maximum flood. The waves create a negative internal pressure on the lee side of the topography. Unlike the eddy where the internal and external pressure anomalies counteract each other, here, the external pressure anomaly is relatively small and often negative like the internal pressure anomaly. When eddies are present along the ridge transects, they can drastically change the pressure field and confine the internal wave to a smaller extent along the transect.

## 4. Implications for Form Drag and Power

The pressure fields described in section 3 can be integrated to get the form drag (10) and power (11), thereby allowing us to quantify the relative contributions to tidal energy loss from the eddies and internal


© 2014. American Geophysical Union. All Rights Reserved.

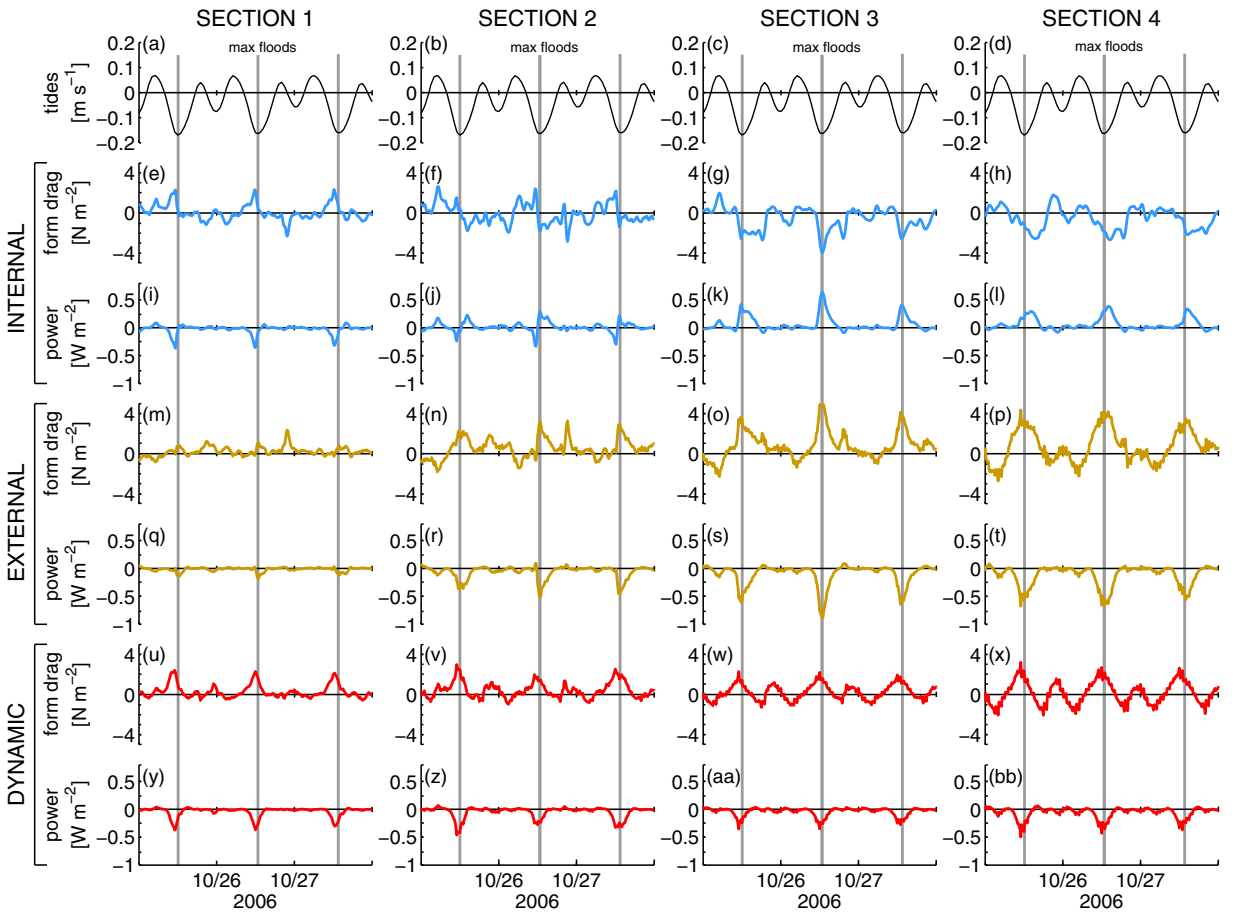


**Figure 8.** (a–d) Time series of tidal currents, (e–h) internal form drag, (i–l) internal power, (m–p) external form drag, (q–t) external power, (u–x) dynamic form drag, and (y–bb) dynamic power along the four analysis sections. The form drag and power have been divided by transect length and are reported in N m$^{-2}$ and W m$^{-2}$, respectively. Maximum strong flood tides are indicated by vertical gray bars. Only 3 days of the model run is shown in order to highlight the details, which repeat themselves every tidal cycle.

waves (Figure 8). The integrated form drag and power along each transect line has been divided by the length of the transect line to get units of N m$^{-2}$ and W m$^{-2}$.

The internal form drag and power change sign from offshore to onshore. Along section 1, the internal form drag (Figure 8e) is generally positive during the first half of strong flood tides and close to zero at other times. There are corresponding negative peaks in internal power during the first half of flood tide (Figure 8i). The one exception occurs at the end of 10/26, when an eddy crosses this transect resulting in negative internal and positive external form drags. In contrast to section 1, along sections 3 and 4, the internal form drag is negative during flood tides (Figures 8g and 8h), and the internal power is positive (Figures 8k and 8l). Transect 2 has a combination of the offshore and onshore dynamics (Figures 8f and 8j). The form drag is positive in the first half of the flood tide when the dynamics are governed by an internal lee wave, and negative in the second half of flood tide when an eddy moves onto the transect and dominates the signal of the internal wave. This interaction of internal waves and eddies leads to internal power that changes sign during flood tides along transect 2.

The external form drag is positive along all four transects (Figures 8m, 8n, 8o, and 8p) leading to negative peaks of power during strong flood tides (Figures 8q, 8r, 8s, and 8t). The external form drag is much larger for the eddy than it is for the internal wave, and therefore it has bigger amplitudes along transects 3 and 4 than along transects 1 and 2.

The dynamic form drag and power have similar amplitudes from transect to transect despite the different behavior of the internal and external parts of the signal. Along all four transects, peaks in power of


© 2014. American Geophysical Union. All Rights Reserved.

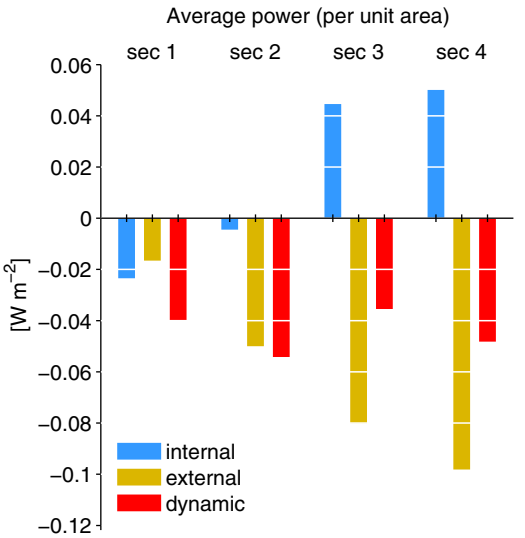


**Figure 9.** Time averaged internal, external, and dynamic powers along the four transects.

$-0.4$ W m$^{-2}$ occur during strong flood tides and the power is close to zero at other times (Figures 8y, 8z, 8aa, and 8bb). Along transect 1, the internal and external powers have the same sign and augment each other. Along transects 3 and 4, the internal and external powers have larger magnitudes than along transect 1, but the signs are opposite, and the dynamic power ends up having nearly the same size as it does along transect 1. Overall, in regions where internal waves dominate, the internal and external powers act together to produce dynamic form drag, whereas in regions where the eddy dominates, they act against each other. It should be noted that the internal and external pressures arise as part of our pressure decomposition (7) and do not physically exist without each other. It is the dynamic pressure that encompasses the physically relevant form drag felt by the fluid.

*Warner et al*. [2013] showed that the form drag at TTP is under-predicted by a bluff body drag law and that a wave drag law works much better because it takes into account the effects of stratification. The magnitude of the form drag and power along the four transects are found to compare much closer to a wave drag law than a bluff body drag law [*Warner et al*., 2013, equations (14) and (13)].

The internal, external, and dynamic powers are time-averaged to get an overall picture of the energy conversion at TTP (Figure 9). The internal power is negative along section 1 and increases to be positive along section 4. Its sign reverses as the dominance of internal waves is overcome by eddies toward shore. The external power is negative along all four transects, its magnitude increasing toward shore. Due to the opposite trends of the internal and external average powers, the time-averaged dynamic power remains nearly constant across the topography at $-0.044 \pm 0.008$W m$^{-2}$. In the observational study of TTP, *Warner et al*. [2013] found an average power of $-0.2$ W m$^{-2}$. The model estimate is low because the velocity in the model is slower than the measured velocity as explained in Appendix A. By increasing the model velocity to match the observed velocity, the average power scales to $-0.11$ W m$^{-2}$. This estimate is still smaller than the observed power possibly because of topographic smoothing in the model. Furthermore, the model grid is large enough to resolve the form drag at TTP as a whole, but subgrid scale processes such as regions of increased drag due to bottom roughness and nonhydrostatic mixing are not resolved within our model. Despite the difference in magnitude of the average power, the pressure and form drag dynamics of the model are qualitatively similar to those observed (Appendix A).

The power losses at TTP are similar to other coastal rough topography. *Osborne et al*. [2011] found time-averaged barotropic to baroclinic tidal energy conversion on the Oregon shelf in regions of rough topography to exceed 0.04 W m$^{-2}$. *Kang and Fringer* [2012] found time-averaged barotropic to baroclinic conversion along the California shelf near and within the Monterey Canyon to reach 0.2 W m$^{-2}$ over rough topography. In a model of the Hawaiian Ridge, *Carter et al*. [2008] found much larger conversion, with spatial peaks of 3 W m$^{-2}$.

*Warner et al*. [2013], found that the internal power made up 80% of the total power along the ridge transect. In the model, it was found that the internal power makes up to $<$10% of the dynamic power along transect 2 which is in the same location as the ridge transect in the observations. The physical reason that there is not as much internal drag along transect 2 in the model is because the eddy often encroaches on the southern end of the transect during flood tides. Due to smoothing of the topography within the model, it is possible that the eddy takes a different path in the model than it does in reality. Since the eddy carries such a large pressure anomaly, it is possible that section 2 in the model is much more influenced by the eddy than the ridge transect was in the observations by *Warner et al*. [2013]. In a different field study at TTP,


© 2014. American Geophysical Union. All Rights Reserved.

*Pawlak et al*. [2003] show that eddies did not cross transect 2 in a series of drifter observations. Along transect 1, the internal power makes up to 60% of the dynamic power which is much closer to what was observed along the ridge transect in *Warner et al*. [2013].

Ideally, we would like to know how to predict whether topography will generate internal waves or eddies. *Klymak et al*. [2010a] show that for large obstacles with topographic Froude numbers, $Nh_m/U_0 > 3$, "partial blocking" occurs and some of the water upstream never surmounts the crest. Here $N$ is the buoyancy frequency, $h_m$ is the topographic height, and $U_0$ is the tidal velocity. Due to the sloping nature of TTP, the flow is not necessarily blocked because it can go around the topography. Along the four transects at TTP, $Nh_m/U_0$ is 1.25 along transect 1, 2.5 along transect 2, and 5 along transects 3 and 4. Transect 2 is just at the point where internal waves are starting to be dominated by eddies. Therefore, we see a very similar response to the parameter space discussed by *Klymak et al*. [2010a]: when $Nh_m/U_0 > 3$, the flow cannot go over the topographic crest and eddies rather than internal waves are formed. *MacCready and Pawlak* [2001] determined that the cutoff between flowing around rather than over sloping topography occurs when $U_0/LNsin(a)=0.5$, where $L$ is the along-slope length of the topography and $a$ is the topographic slope. At TTP, $U_0/LNsin(a)=0.3$, which means that currents should go over rather than around topography, generating internal waves. This parameter, however, does not take into account the depth of the water column. At TTP, the fact that the topography rises out of the water means that the parameter $h_m/H$, where $H$ is the total water column depth, must also play a role because internal waves cannot occur in places where the topography rises up through the majority of the water column. At TTP, the transition from internal waves to eddies occurs at the point where $h_m/H \approx 0.5$. Further investigation into the importance of these parameters over a wide range of topography would be needed to determine the exact parameter space where transition from internal waves to eddies occurs on sloping topography.

## 5. Conclusions

In this study, a numerical model of Three Tree Point was used to gain insight into the physical mechanisms that create form drag across this sloping headland. The part of the bottom pressure field that contributes to form drag was divided into the internal and external pressures so the eddies and internal waves could be identified. It was found that internal waves are the dominant mechanism along the ridge-like part of the topography and eddies are the dominant mechanism closer to shore. Both the internal waves and eddies are largest during strong flood tides and much weaker during the small flood or ebb tides.

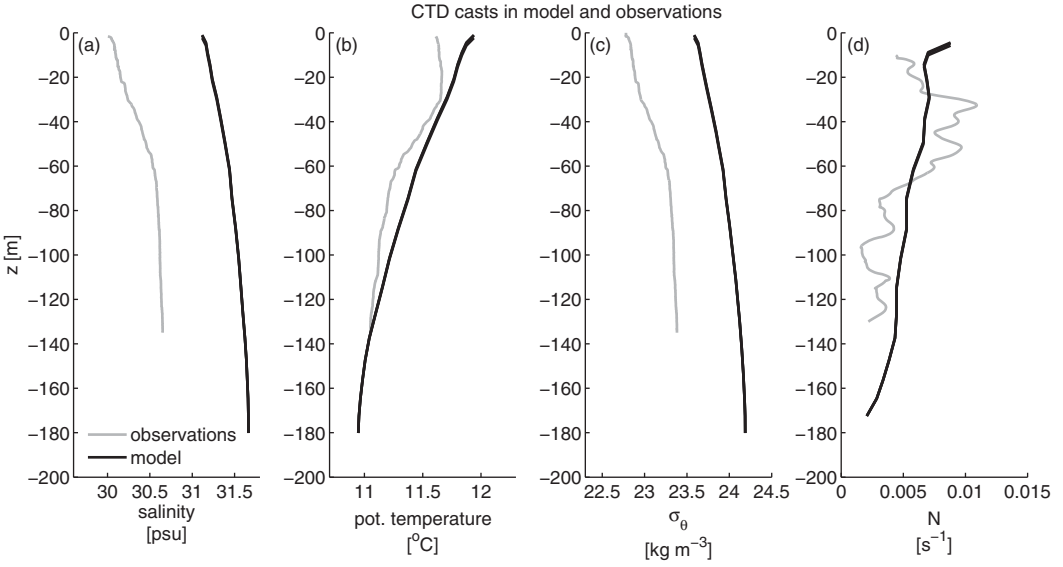


**Figure 10.** (a) Salinity from the observations averaged over the time period of the cruise in 2010 [*Warner et al*., 2013] (gray) and from model averaged over the week in 2006 during which the model was run (black). (b) Potential temperature. (c) Potential density. (d) Buoyancy frequency.


© 2014. American Geophysical Union. All Rights Reserved.

In regions where internal waves dominate, internal, and external pressures work in concert to create dynamic pressure that is larger than either individual part. The average dynamic power is made up of 60% internal power and 40% external power. The dynamics are complicated in the internal wave regime when eddies are pushed into this part of the domain affecting the bottom pressure anomalies and confining the internal lee wave to a smaller region along the topography.

The tilted nature of the eddies leads to a complicated pattern of internal and external pressures. In the top half of the eddy, the external pressure is negative and the internal pressure is positive, which leads to a dynamic bottom pressure that is nearly zero except right next to the shore where isopycnals have limited vertical excursions. In the bottom half of the eddy, which can be located nearly 2 km from the surface of the eddy, both the internal and external pressures tend to be negative. However, the bottom of the eddy is often located over flat parts of topography and therefore does not contribute significantly to form drag. Overall, in the regions where

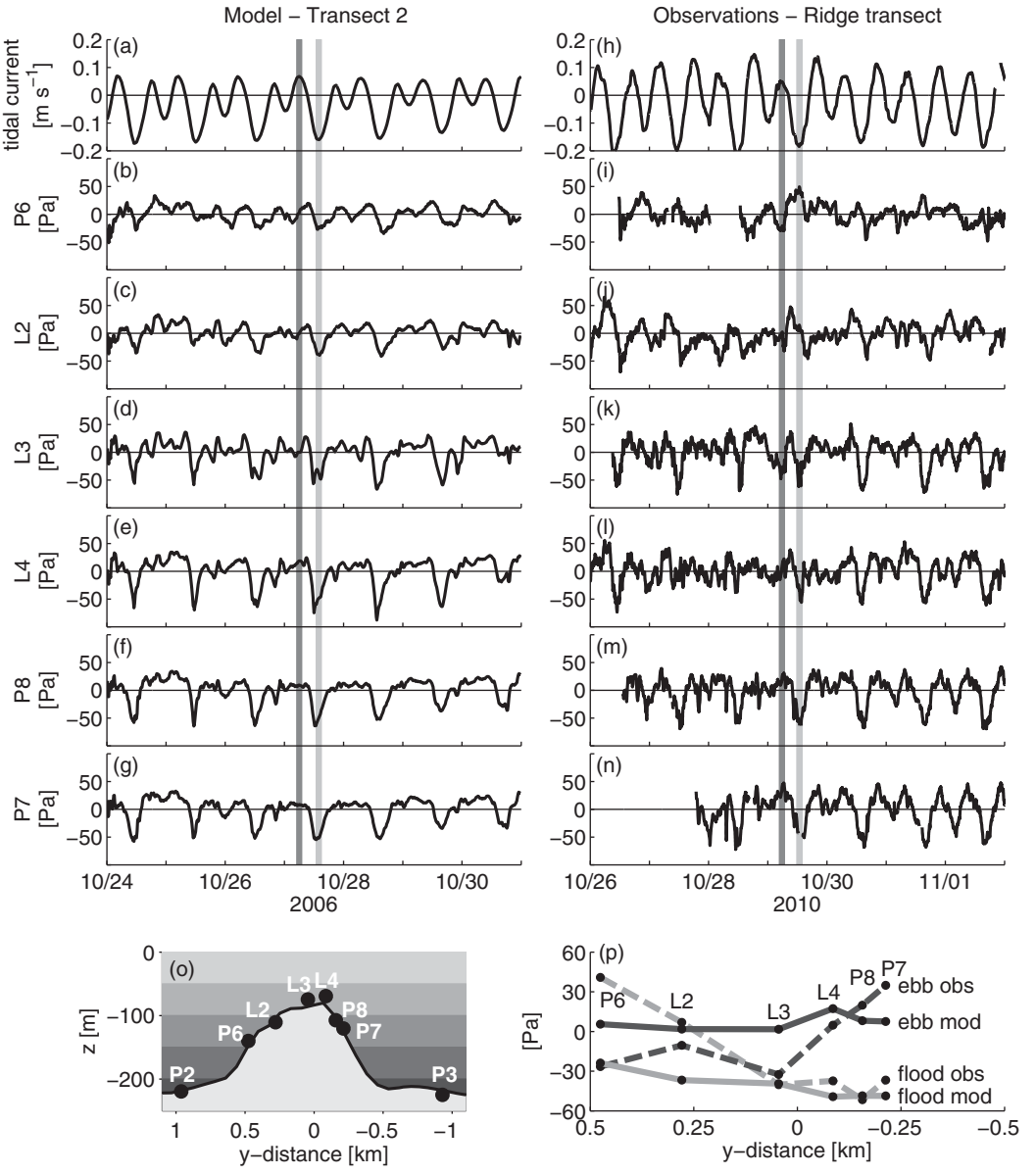


**Figure 11.** (a) Model tides. Vertical bars highlight 2 h spanning maximum flood (light gray) and maximum ebb (dark gray). (b–g) Bottom pressure anomalies from the model on transect 2. Locations in (o). (h) Observed tides from *Warner et al.* [2013]. (i–n) Observed bottom pressure anomalies. (p) Average bottom pressure anomalies plotted with respect to distance from the topographic crest during ebb (dark gray) and flood (light gray) for both the model (solid lines) and the observations (dashed lines).


© 2014. American Geophysical Union. All Rights Reserved.

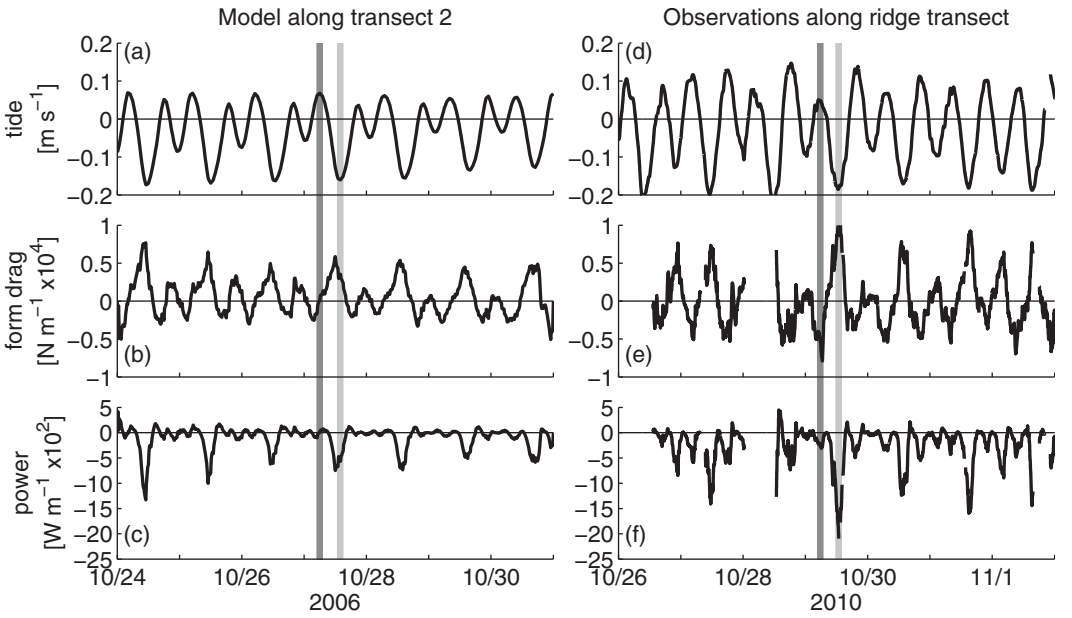


**Figure 12.** (a) Tidal currents from the model. Vertical bars indicate 2 h window spanning max flood (light gray) and max ebb (dark gray). (b) Form drag and (c) power from transect 2 in the model. (d) Tidal currents from the observations [*Warner et al*., 2013]. (e) Observed form drag and (f) power from the ridge transect.

eddies dominate, the internal power tends to be positive and the external power tends to be negative. Together, they lead to a dynamic power that is also negative but only about half as big as the external power.

Even though the internal and external pressure anomalies of the eddy have much bigger magnitudes than the pressure anomalies from the internal wave, both processes do similar amounts of work. The dynamic power loss has peaks of 0.4 W m$^{-2}$ across the topography which equivalent to a time average of 0.04 W m$^{-2}$. Scaled to account for the slower velocity in the model than at the real TTP gives a time-averaged power loss of 0.11 W m$^{-2}$. This is much larger than losses due to friction.

Overall, this study shows the complicated dynamics that occur when both internal waves and eddies are created by sloping topography. The eddies are tilted and have a pressure anomaly structure that is different from vertical eddies. The internal lee waves are created on the ridge-like part of the topography and can be suppressed by the presence of an eddy. Both phenomena contribute nearly equally to form drag in the region. Combined, they lead to a bottom pressure anomaly field that differs significantly from that found near topography that generates just internal waves or eddies alone.

## Appendix A: Model Compared to Observations

The goal of this paper is not to directly compare the TTP model to the field observations that are detailed in *Warner et al*. [2013], but instead to gain insight into the physical mechanisms that create form drag. Differences are expected between the model and observations simply because they cover different time periods (model: 24–31 October 2006 and observations: 26 October to 2 November 2010). Furthermore, the model bathymetry had to be smoothed (Figure 1e). Despite this, we compare the model to the observations so we know what the model does and does not do well.

### A1. Density

The model is too salty by about 1 psu (Figure 10a), which is a known defect of the MoSSea model [*Sutherland et al*., 2011]. This leads to potential density within the model that is about 0.75 kg m$^{-3}$ too high (Figure 10c). The potential temperature in the model is similar to the observed (Figure 10b). Despite the differences in salinity and density, the buoyancy frequency is generally the same (Figure 10d). Differences in stratification could affect how easy it is for water to flow over versus around the topography. As the buoyancy


© 2014. American Geophysical Union. All Rights Reserved.

frequency increases, it is more likely for the flow to be around the topography than over it [*MacCready and Pawlak*, 2001].

### A2. Tidal Currents

The time period of the model was chosen to match the tides from the observations as closely as possible, however, there are some differences between the two, most notably in their amplitude (Figures 11a and 11h). The maximum velocity during flood tides in the model and observations are 0.17 and 0.23 m $s^{-1}$, respectively. The reason for this disparity is due to the weak $M_2$ tidal currents in the MoSSea Model [*Sutherland et al*., 2011]. Due to weaker tides, it is expected that the form drag and power will not be as big as the observations. Nonetheless, the form drag is still many times greater than the frictional drag.

### A3. Bottom Pressure Anomalies

Bottom pressure anomalies from the model and observations can be compared at the locations of the pressure sensors (Ppods) from the field study (Figure 11). There are similar patterns between the two. The pressure anomalies on the north side of TTP (Figures 11b, 11c, 11i, and 11j) are smaller than the pressure anomalies on the crest (Figures 11d, 11e, 11k, and 11l) and south side (Figures 11f, 11g, 11m, and 11n). The magnitude of the bottom pressure anomalies on the south side during strong flood tides is quite large, whereas during ebb and weak flood tides, the signal is much smaller. In both the model and observations, the bottom pressure anomaly decreased from north to south during flood tides (Figure 11o). However, that decrease is about four times greater in the observations (change of 100 Pa) than in the model (change of 25 Pa). During ebb tides, the pressure increased from north to south in the observations (change of 60 Pa), whereas, in the model, there is only a slight increase in pressure anomalies across the topography during ebb tide. Overall, the amplitude of the bottom pressure anomalies is too small in the model, but the patterns of high and low pressures are similar between the model and observations.

### A4. Form Drag and Power

Both the observations and model (Figure 12) show largest peaks of form drag (10) and power (11) at maximum flood tides and much smaller peaks during ebbs and weak floods. The observed amplitude is larger than the modeled. The average observed power is 248 W $m^{-1}$ and the average model power is 100 W $m^{-1}$. Based on the differences between modeled and observed tidal velocities, and a form drag that varies as $v_0^2$, we would predict that the model would only account for 40% of the observed power, consistent with the results above.

**Acknowledgments**

Thank you to David Darr, David Sutherland, and the MoSSea Users Group for valuable help in setting up and running the numerical model. Thank you to Jim Moum and Jonathan Nash for orchestrating the field work at Three Tree Point. Matthew Alford, LuAnne Thompson, and two anonymous reviewers provided many helpful suggestions for improving this paper. This work was funded by NSF Awards OCE-0751683 and OCE-0751930.

## References

Arbic, B. K., A. J. Wallcraft, and E. J. Metzger (2010), Concurrent simulation of the eddying general circulation and tides in a global ocean model, *Ocean Modell.*, *32*(3–4), 175–187, doi:10.1016/j.ocemod.2010.01.007.

Baines, P. G. (1995), *Topographic Effects in Stratified Flows*, Cambridge Univ. Press, Cambridge, U. K.

Black, K. P., and S. L. Gay (1987), Eddy formation in unsteady flows, *J. Geophys. Res.*, *92*(C9), 9514–9522.

Boyer, D. L., and L. Tao (1987), On the motion of linearly stratified rotating fluids past capes, *J. Fluid Mech.*, *180*, 429–449.

Callendar, W., J. M. Klymak, and M. G. G. Foreman (2011), Tidal generation of large sub-mesoscale eddy dipoles, *Ocean Sci.*, *7*(4), 487–502, doi:10.5194/os-7–487-2011.

Canals, M., G. Pawlak, and P. MacCready (2009), Tilted baroclinic tidal vortices, *J. Phys. Oceanogr.*, *39*(2), 333–350.

Canuto, V. M., A. Howard, Y. Cheng, and M. S. Dubovikov (2001), Ocean turbulence. Part I: One-point closure model—Momentum and heat vertical diffusivities, *J. Phys. Oceanogr.*, *31*, 1413–1426.

Carter, G. S., M. A. Merrifield, J. M. Becker, K. Katsumata, M. C. Gregg, D. S. Luther, M. D. Levine, T. J. Boyd, and Y. L. Firing (2008), Energetics of $M_2$ barotropic-to-baroclinic tidal conversion at the Hawaiian Islands, *J. Phys. Oceanogr.*, *38*, 2205–2223, doi:10.1175/2008JPO3860.1.

Cenedese, C., and J. A. Whitehead (1999), Eddy shedding from a boundary current around a cape over a sloping bottom, *J. Phys. Oceanogr.*, *30*, 1514–1521.

Chapman, D. C. (1985), Numerical treatment of cross-shelf open boundaries in a barotropic coastal ocean model, *J. Phys. Oceanogr.*, *15*, 1060–1075.

Edwards, K. A., P. MacCready, J. N. Moum, G. Pawlak, J. Klymak, and A. Perlin (2004), Form drag and mixing due to tidal flow past a sharp point, *J. Phys. Oceanogr.*, *34*, 1297–1312.

Farmer, D., and L. Armi (1999a), The generation and trapping of solitary waves over topography, *Science*, *283*(5398), 188–190.

Farmer, D. M., and L. Armi (1999b), Stratified flow over topography: The role of small-scale entrainment and mixing in flow establishment, *Proc. R. Soc. London, Ser. A*, *455*, 3221–3258.

Finlayson, D. P. (2005), *Combined Bathymetry and Topography of the Puget Lowland*, Univ. of Washington, Seattle, Wash. [Available at: http://www.ocean.washington.edu/data/pugetsound/psdem2005.html.]

Flather, R. A. (1976), A tidal model of the northwest European continental shelf, *Mem. Soc. R. Sci. Liege*, *10*, 141–164.

Garrett, C., and E. Kunze (2007), Internal tide generation in the deep ocean, *Annu. Rev. Fluid Mech.*, *39*(1), 57–87.

Geyer, W. R., and R. Signell (1990), Measurements of tidal flow around a headland with a shipboard acoustic Doppler current profiler, *J. Geophys. Res.*, *95*(C3), 3189–3197.


© 2014. American Geophysical Union. All Rights Reserved.

Gill, A. E. (1982), *Atmosphere-Ocean Dynamics*, Academic, San Diego, Calif.
Jayne, S. R. (2009), The impact of abyssal mixing parameterizations in an ocean general circulation model, *J. Phys. Oceanogr.*, *39*(7), 1756–1775, doi:10.1175/2009JPO4085.1.
Jayne, S. R., and L. C. St. Laurent (2001), Parameterizing tidal dissipation over rough topography, *Geophys. Res. Lett.*, *28*(5), 811–814.
Kang, D., and O. Fringer (2012), Energetics of barotropic and baroclinic tides in the Monterey Bay area, *J. Phys. Oceanogr.*, *42*, 272–290.
Kelly, S. M., J. D. Nash, and E. Kunze (2010), Internal-tide energy over topography, *J. Geophys. Res.*, *115*, C06014, doi:10.1029/2009JC005618.
Klinger, B. A. (1994), Baroclinic eddy generation at a sharp corner in a rotating system, *J. Geophys. Res.*, *99*(C6), 12,515–12,531.
Klymak, J. M., and M. C. Gregg (2001), Three-dimensional nature of flow near a sill, *J. Geophys. Res.*, *106*(C10), 22,295–22,311.
Klymak, J. M., and M. C. Gregg (2003), The role of upstream waves and a downstream density pool in the growth of lee waves: Stratified flow over the Knight Inlet Sill, *J. Phys. Oceanogr.*, *33*, 1446–1461.
Klymak, J. M., S. M. Legg, and R. Pinkel (2010a), High-mode stationary waves in stratified flow over large obstacles, *J. Fluid Mech.*, *644*, 321–336.
Klymak, J. M., S. Legg, and R. Pinkel (2010b), A simple parameterization of turbulent tidal mixing near supercritical topography, *J. Phys. Oceanogr.*, *40*(9), 2059–2074, doi:10.1175/2010JPO4396.1.
Lavelle, J. W., H. O. Mofjeld, E. Lempriere-Doggett, G. A. Cannon, D. J. Pashinski, E. D. Cokelet, L. Lytle, and S. Gill (1988), A multiply-connected channel model of tides and tidal currents in Puget Sound, Washington and a comparison with updated observations, *Tech. Rep. ERL PMEL-84*, NOAA Pac. Mar. Environ. Lab., Seattle, Wash.
Legg, S., and K. M. H. Huijts (2006), Preliminary simulations of internal waves and mixing generated by finite amplitude tidal flow over isolated topography, *Deep Sea Res., Part II*, *53*, 140–156.
Li, C., S. Armstrong, and D. Williams (2006), Residual eddies in a tidal channel, *Estuaries Coasts*, *29*(1), 147–158.
MacCready, P., and G. Pawlak (2001), Stratified flow along a rough slope: Separation drag and wave drag, *J. Phys. Oceanogr.*, *31*, 2824–2839.
McCabe, R., P. MacCready, and G. Pawlak (2006), Form drag due to flow separation at a headland, *J. Phys. Oceanogr.*, *36*, 2136–2152.
Nakamura, T., T. Awaji, T. Hatayama, K. Akitomo, and T. Takizawa (2000), The generation of large-amplitude unsteady lee waves by subinertial K1 tidal flow: A possible vertical mixing mechanism in the Kuril Straits, *J. Phys. Oceanogr.*, *30*, 1601–1621.
Nash, J. D., and J. N. Moum (2001), Internal hydraulic flows on the continental shelf: High drag states over a small bank, *J. Geophys. Res.*, *106*(C3), 4592–4612.
Niwa, Y., and T. Hibiya (2011), Estimation of baroclinic tide energy available for Deep Ocean mixing based on three-dimensional global numerical simulations, *J. Oceanogr.*, *67*, 493–502.
Oke, P. R., and D. A. Griffin (2011), The cold-core eddy and strong upwelling off the coast of New South Wales in early 2007, *Deep Sea Res., Part II*, *58*(5), 574–591, doi:10.1016/j.dsr2.2010.06.006.
Osborne, J. J., A. L. Kurapov, G. D. Egbert, and P. M. Kosro (2011), Spatial and temporal variability of the m2 internal tide generation and propagation on the Oregon shelf, *J. Phys. Oceanogr.*, *41*(11), 2037–2062, doi:10.1175/JPO-D-11-02.1.
Pawlak, G., and P. MacCready (2002), Oscillatory flow across an irregular boundary, *J. Geophys. Res.*, *107*(C5), 4–1–4–7, doi:10.1029/2000JC000596.
Pawlak, G., P. MacCready, K. A. Edwards, and R. McCabe (2003), Observations on the evolution of tidal vorticity at a stratified deep water headland, *Geophys. Res. Lett.*, *30*(24), 2234, doi:10.1029/2003GL018092.
Pingree, R. D., and L. Maddock (1979), The tidal physics of headland flows and offshore tidal bank formation, *Mar. Geol.*, *32*, 269–289.
Shchepetkin, A. F., and J. C. McWilliams (2005), The Regional Oceanic Modeling System (ROMS): A split-explicit, free-surface, topography-following-coordinate oceanic model, *Ocean Modell.*, *9*, 347–404.
Signell, R. P., and W. R. Geyer (1991), Transient eddy formation around headlands, *J. Geophys. Res.*, *96*(C2), 2561–2575.
Sutherland, D. A., P. MacCready, N. S. Banas, and L. F. Smedstad (2011), A model study of the Salish Sea estuarine circulation, *J. Phys. Oceanogr.*, *41*(6), 1125–1143.
Umlauf, L., and H. Burchard (2003), A generic length-scale equation for geophysical turbulence models, *J. Mar. Res.*, *61*, 235–265.
Warner, S. J., and P. MacCready (2009), Dissecting the pressure field in tidal flow past a headland: When is form drag ''real''?, *J. Phys. Oceanogr.*, *39*(11), 2971–2984.
Warner, S. J., P. MacCready, J. N. Moum, and J. D. Nash (2013), Measurement of tidal form drag using seafloor pressure sensors, *J. Phys. Oceanogr.*, *43*, 1150–1172.
White, L., and E. Wolanski (2008), Flow separation and vertical motions in a tidal flow interacting with a shallow-water island, *Estuarine Coastal Shelf Sci.*, *77*, 457–466.


© 2014. American Geophysical Union. All Rights Reserved.